

Spectroscopy and trapping dynamics in WS₂ nanoclusters

J. M. Huang,^{1,*} R. A. Laitinen,² and D. F. Kelley^{1,2,†}

¹*Department of Chemistry, Kansas State University, Manhattan, Kansas 66506-3701*

²*Department of Chemistry, Colorado State University, Fort Collins, Colorado 80523*

(Received 27 January 2000)

WS₂ nanoclusters have been synthesized using inverse micelle methods and characterized by TEM, electron diffraction, and optical spectroscopy. The TEM images and rotational diffusion results show that the particles have average diameters of approximately 4–7 nm and have the same crystal structure as bulk WS₂. The electron diffraction results are compared with diffraction patterns calculated as a function of the nanocluster diameter and thickness. This comparison shows that the particles are single trilayer disks. The absorption spectrum shows a large blue shift compared to bulk WS₂, with the first absorption maximum shifting from about 680 nm to 364 nm. Polarized emission is observed following photoexcitation. The emission polarization spectra indicate that absorption occurs into several different low-lying states. The results also indicate that emission from the band-edge state is polarized, while emission from trap states is not. The dynamics of these nanoclusters in room temperature solutions have been examined using time-resolved emission and polarization spectroscopies. Trap-state emission exhibits multiexponential distributed kinetics, while emission from the band-edge state follows a single exponential decay. In samples having a high density of subband-gap trap states, the vast majority of the emission is from trap states. In samples in which most of the traps have been passivated, most of the emission is from the band-edge state. Time-resolved emission polarization measurements indicate that trapping takes place on the 100 ps time scale, and that the trapping rate depends on the density of trap states.

INTRODUCTION

The optical and electronic properties of semiconductor nanoclusters have recently been of great interest.¹ This is largely due to the phenomenon of quantum confinement, whereby in sufficiently small particles, the spectroscopic properties depend strongly on the particle size. When the spatial extent of photogenerated excitons is comparable to the dimensions of the nanocluster, quantum confinement effects are observed. These effects may be very large, and the nanocluster band gap may be more than an electron volt larger than that of the bulk semiconductor. Quantum confinement effects may be semiquantitatively described by “effective mass” models of the photogenerated electron/hole pair.^{2–6} In addition to changing the observed band gap, quantum confinement can also dramatically affect the distribution of electronic states. Electronic states in the conduction and valence bands are normally thought of as being a continuum. However, this is not the case in a strongly quantum confined semiconductor nanocluster. In this case, quantum confinement results in both the conduction and valence bands becoming a discrete set of states; the “band” structure is lost. The resulting nanocluster electronic structure consists of a set of delocalized states which correlate to the conduction and valence bands of the bulk semiconductor. For clarity, however, we will refer to the lowest energy delocalized state as the band-edge state, in spite of the fact that these states are widely separated and discrete, rather than a continuous band.

Surface atoms of semiconductor nanoclusters typically have “dangling bonds” which result in localized electron and hole states. If the energy of these states is below that of the band edge, then they may act as electron and hole traps. For clarity, we will refer to all of these localized states as

trap states. The trap states can dominate the recombination dynamics of photogenerated electron/hole pairs. It is often possible to passivate the surface traps by reaction with surface derivatizing agents or by coating the nanocluster with a larger band gap semiconductor having a commensurate lattice structure.^{7–16} Several studies have shown that passivation of surface traps has large effects on the nanocluster spectroscopy and photophysics.^{17–20} Radiative recombination of trapped electron/hole pairs typically results in broad, unstructured emission, and a fairly low emission quantum yield. In cases where the surface traps are passivated, intense band-edge emission is typically observed.

The layered metal dichalcogenides (MX₂, M=Mo,W, and X=S,Se) are of particular interest for the study of the dynamical effects of quantum confinement. This is because these materials exhibit large quantum confinement effects in their spectroscopy and because they exhibit very weak electron/phonon coupling. The weak electron/phonon coupling may be understood in terms of their bonding.²¹ The band gap transition largely corresponds to moving an electron from one set of nonbonding orbitals to another. All of these materials have very similar structural and electronic properties. They crystallize into a hexagonal layered structure (*P6₃/mmc-D_{6h}⁴*), with similar lattice constants.²² This layered structure consists covalently bound S-W-S trilayers, separated by a relatively large van der Waals gap. The different polytypes of WS₂ differ only in how the trilayers stack on each other. All of these materials are indirect bandgap semiconductors, with similar direct and indirect band gaps. WS₂ has indirect and direct band gaps of 1.35 and 1.74 eV, respectively, as determined by photocurrent spectroscopy.²³ The dominant features in the absorption spectra are assigned to transitions which are polarized perpendicular to the crys-

tallographic c axis. For example, the lowest energy direct exciton transitions (the A and B excitons) are polarized perpendicular to the c axis. However, several perpendicularly polarized features at comparable energies are seen in single crystal reflection spectra.^{24–26}

Despite being well suited for spectroscopic and dynamical studies, a limited amount of work on nanoclusters of these materials has been done, with most of the existing work having been done on MoS₂ nanoclusters. MoS₂ nanoclusters with diameters reported to be from 2.5 to 4.5 nm have been synthesized. The smallest (2.5 nm) and larger (4.5 nm) MoS₂ nanoclusters show lowest energy absorbance maxima at 360 and 470 nm, respectively.²⁷ These peaks are assigned to the lowest energy direct exciton, which occurs at 680 nm in the bulk material.²⁴ MoS₂ nanoclusters exhibit emission with a quantum yield of about 10^{-4} , following photoexcitation at room temperature. The emission is broad and structureless, and is thus assigned to radiative electron/hole recombination from the trap states. The emission kinetics are strongly non-exponential, and may be described in terms of a distributed kinetics model.²⁸ The kinetics are accurately fit if the Bohr radius of the trapped electron is taken to be 2.0–2.5 nm, which is comparable to the known MoS₂ exciton radius.²⁴ Band-edge emission has also been observed in MoS₂ nanoclusters following trap passivation and at low (<40 K) temperatures. Unlike emission from trap states, band-edge emission follows single exponential kinetics.²⁸ Dynamical studies of electron transfer at MoS₂ nanocluster interfaces have also been reported.^{29–31}

The absorption spectrum of WS₂ nanoclusters has also been reported, but none of the synthetic details or characterization of these particles were given.^{27(b)} In the present paper, we report the synthesis and characterization of WS₂ nanoclusters. We also examine the spectroscopy and kinetics of trap state and band-edge emission in these nanoclusters. We show that both the band-edge state and the trap states are comparatively long lived and that band-edge emission dominates the spectrum following trap passivation. We also show that the lowest indirect transition has an onset which is buried under the more intense and better resolved lowest direct transition. A wealth of information about the excited states of the nanocluster can be obtained from polarization spectroscopy. Polarization of the band-edge emission can arise from the crystal structure and/or the morphology of the nanocluster. In the case of CdSe nanoclusters, for example, it is the anisotropic crystal structure which gives rise to polarized emission.³² In the present paper we examine the polarized emission spectroscopy of WS₂ nanoclusters. The results indicate that the lowest energy allowed transitions in the nanoclusters do not correlate to the lowest direct exciton transitions (A and B excitons) of bulk WS₂. We also examine the rates of band edge to trap state relaxation and of nonradiative electron/hole recombination from the band-edge state.

EXPERIMENT

Tungsten(IV)sulfide nanoclusters were synthesized by methods similar to those described previously with molybdenum(IV)sulfide.^{27–29} Tungsten(IV)chloride was obtained from Aldrich and was repeatedly washed with carbon

tetrachloride in an inert atmosphere drybox to remove undesired tungsten oxychlorides. The WCl₄ was then dissolved in a degassed ternary tridodecylmethyl ammonium iodide (TDAI)/hexanol/octane (8/8/84 by weight) inverse micelle solution, at a concentration of 1.0×10^{-3} M. To this rapidly stirring solution was added 4.0 molar equivalents of H₂S via gas-tight syringe. Following H₂S addition and resulting WS₂ nucleation, the mixture was allowed to stir for 30 min. WCl₄ is much less reactive toward H₂S than is MoCl₄ and WS₂ nanocluster growth is not complete in this amount of time. At this point in the nanocluster growth, the inverse micelle solution is extracted with acetonitrile. The nanoclusters partition between the nonpolar octane phase and the polar acetonitrile/TDAI/hexanol phase. The resulting nanoclusters in both polar and nonpolar phases continue to grow for about the 24 to 48 h. Alternatively, nanocluster growth may be allowed to occur in the inverse micelles, followed by extraction into acetonitrile. Similar results are obtained in both cases. The WS₂ nanoclusters in the acetonitrile phase may also be extracted into a clean octane layer by the addition of a very small quantity of water. The resulting nanoclusters exhibit spectra and dynamics which are almost identical to those grown in the octane phase.

TEM images and electron diffraction results were obtained on a Philips CM-100 transmission electron microscope. Samples were prepared by diluting the nanocluster octane solution (extracted from the acetonitrile solution) by a factor of 5 with octane, and evaporating a drop onto a Formvar grid. These samples have very little TDAI in them, which interferes with the TEM imaging and electron diffraction. For comparison, some nanocluster samples prepared from the acetonitrile phase (having TDAI and hexanol) were also examined.

Time-resolved emission results were obtained by time correlated single photon counting, using an apparatus that has been previously described.³³ In this apparatus, wavelength selection was accomplished using a 1/4 m monochromator with a 150 groove/mm grating. The resulting detection bandwidth was about 10 nm. The temporal resolution was about 75 ps, FWHM. In all cases, the excitation pulse energies were about 1.0 nJ, and were focused to a spot size of about 0.5 mm. This results in fluences that are sufficiently low that multiphoton excitations are completely avoided. Static emission spectra were obtained using a home-built instrument that has been described earlier.^{33(b)} Polarization studies utilized a 1 cm Glan-Taylor excitation polarizer and a Polaroid emission polarizer.

RESULTS AND DISCUSSION

TEM and electron diffraction

Two sets of TEM images of WS₂ nanoclusters are shown in Fig. 1. These images are from two different sections of the same sample, which was prepared by evaporation of a dilute octane sample onto a Formvar grid. The nanoclusters images have fairly low contrast, indicating that they are very thin. This observation is consistent with the nanoclusters consisting of single S-W-S trilayers, as indicated by the electron diffraction results, below. The nanoclusters have irregular shapes with dimensions of about 3.5 to 9 nm, with the average dimensions being about 4–7 nm. This is in good agree-

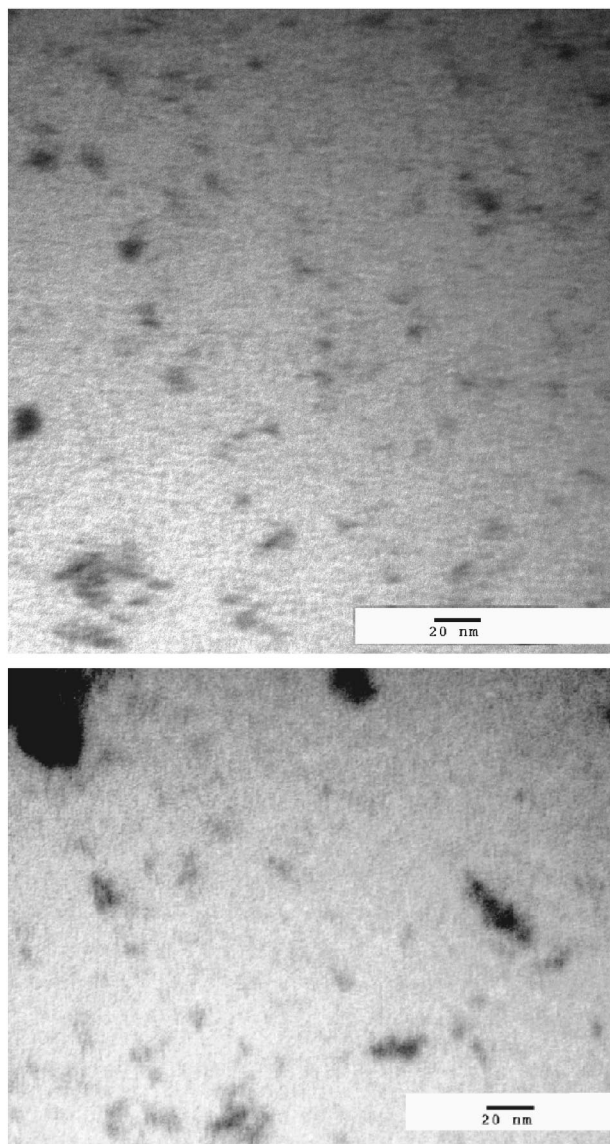


FIG. 1. TEM images of WS₂ nanoclusters having dimensions of approximately 4–7 nm and several nanocluster aggregates.

ment with the average diameter obtained from rotational diffusion measurement, discussed below. We note that some of the apparent irregularity in the nanocluster shapes may be due to the nanoclusters being very thin and not lying flat on the grid. An almost edge-on view will result in what looks like a nanocluster which is much longer than it is wide. Figure 1 also shows several somewhat larger images having higher contrast. The darker image indicates that these particles are thicker, and are assigned to an aggregates. Some aggregation is very difficult to avoid under these sample preparation conditions.

Electron diffraction results and their crystallographic assignments are shown in Fig. 2, and are summarized in Table I. These results were obtained from a large nanocluster aggregate prepared in the same way as the sample as used to obtain the images shown in Fig. 1. Good agreement between the reference values for bulk WS₂ and the observed diffraction angles is obtained in all cases, with two or three notable exceptions. An intense ring is observed at a relative angle of 0.48. This feature cannot be assigned to WS₂, but is domi-

nant in diffraction patterns taken which an excess of surfactant. It may therefore be assigned to some crystallized TDAI, and is of no consequence. More importantly, the 0,0,2 and 0,0,6 rings are completely absent in the observed diffraction pattern. It is of interest to compare these results to calculated diffraction patterns. Calculations were performed for several different assumed nanocluster diameters and thicknesses using Cerius² software. These calculations show that in all cases, the 0,0,6 ring is expected to be weak, so its absence is not surprising. The calculations also show that if the nanocluster is assumed to consist of three or more S-W-S trilayers, then the most intense diffraction ring is the 0,0,2. For the case that the nanocluster is two trilayers thick, the 0,0,2 ring is broadened, but has the second highest intensity, slightly below that of the 1,0,0 ring. A diffraction ring having this intensity would be clearly visible in the diffraction pattern. These considerations indicate that the nanoclusters are single trilayer sheets of WS₂, and that each trilayer has the same structure and close to the same lattice constants as bulk WS₂.

The above considerations allow us to comment on the morphology of WS₂ nanoclusters in solution, and the aggregation that occurs upon solvent evaporation. It is possible to imagine that the individual S-W-S trilayers could undergo aggregation by dimerization or stacking in solution and especially when the solvent is removed. This would be caused solely by van der Waals forces holding adjacent trilayers next to each other. However, in these small nanoclusters, this corresponds to a small binding energy and the entropically favored situation of single trilayer nanoclusters is expected to dominate in dilute solutions. This expectation is consistent with the results of concentration dependent spectroscopic studies. The absorption spectrum is concentration independent down to a nanocluster concentration where the peaks are lost in the background, about of 10⁻⁷ M, suggesting that little or no dimerization occurs. This conclusion is consistent with the recent results on the exfoliation of other layered materials, where individual sheets are observed,^{34,35} and also consistent with our STM results on MoS₂ nanoclusters.³⁶ From these considerations and the diffraction results we conclude that stacking or dimerization does not occur to any significant extent in solution. We also conclude that removal of the solvent results in random nanocluster orientations, rather than ordered arrays.

Band-edge and trap-state spectroscopy

WS₂ nanoclusters in both octane and acetonitrile/TDAI/hexanol phases show nearly identical absorption spectra, with the lowest energy maxima at 364 nm (see Fig. 3). These peaks are quite similar to the peaks seen in PbI₂ nanocluster spectra, which have been controversial.³⁷ Earlier studies indicated that the peaks were due to molecular species rather than nanoclusters, specifically I₃⁻. Due to the presence of I⁻ (from the TDAI) in the present synthesis, this possibility must also be considered here. Two results indicate that the 364 nm and 295 nm peaks are due to WS₂ nanoclusters rather than I₃⁻. First, the blank spectrum (same synthesis, except without the WCl₄) shows no absorbance at wavelengths >280 nm in either acetonitrile or octane phases. Second, introduction of a small amount of I₂ into the blank,

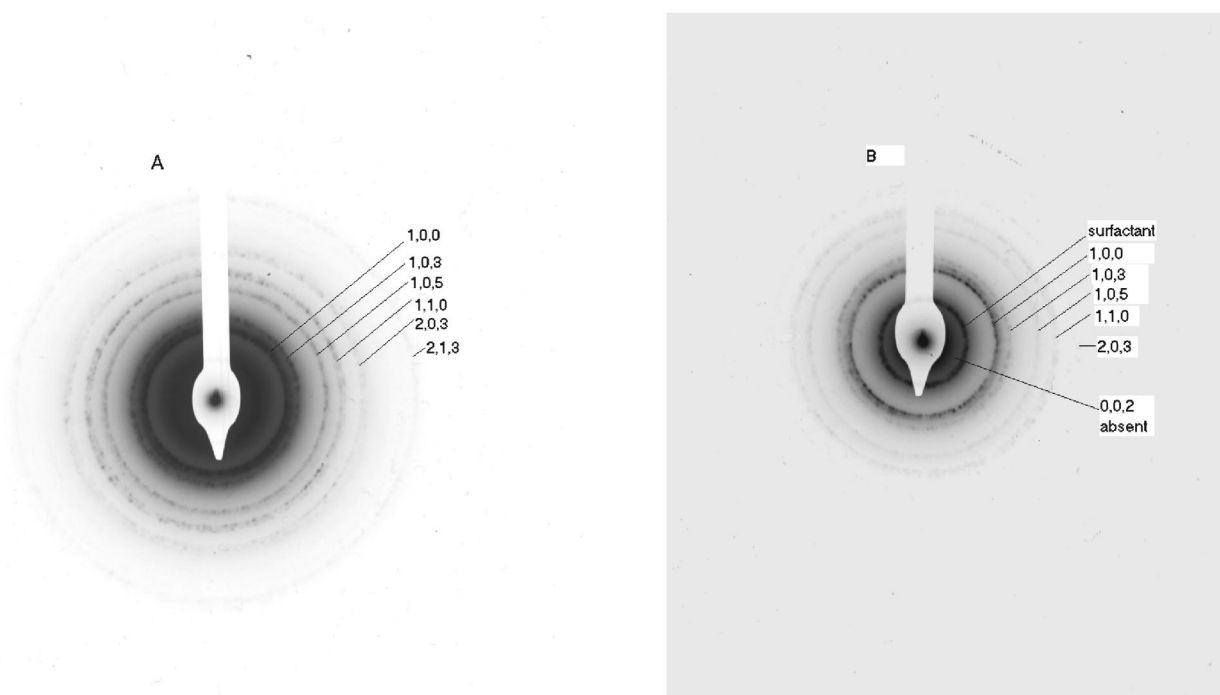


FIG. 2. Electron diffraction results taken from an aggregate of WS_2 nanoclusters. *A* and *B* correspond to longer and shorter exposures of the same diffraction pattern. The inner diffraction rings are more clearly seen in a less exposed image. The assignments are also shown and the results are summarized in Table I. The expected position of the 0,0,2 ring is also indicated.

followed by extraction gives the I_3^- absorption peaks only in the acetonitrile phase; I_3^- is insoluble in the octane phase. These results indicate that while it is possible to get spectral contamination in the acetonitrile phase, this does not happen to a significant extent and the octane phase absorption is due entirely to WS_2 nanoclusters.

These spectra are also remarkably similar to those obtained for MoS_2 nanoclusters.^{27,28} The similarity between the absorption spectra of MoS_2 and WS_2 nanoclusters suggests that either both types of nanoclusters have comparable ex-

tents of quantum confinement, or that some of the absorption is due to surface states which are similar in both systems. In the latter scenario, the polarization results discussed below exclude the possibility that excitation of a surface state results in population of the emissive band edge state. While there is no direct evidence of it, we cannot exclude the possibility that some of the absorption is due to surface states which relax very quickly and therefore result in no emission. The present results establish that the 295 and 364 nm absorption peaks are due to WS_2 nanoclusters, but do not exclude

TABLE I. Electron diffraction results. vs: very strong; m: medium; w: weak; vw: very weak.

Reference angle	Relative intensity	Assignment	Observed displacement	Relative angle	Observed intensity
0.344	100	0,0,2			absent
		surfactant	1.00	0.48	vs
0.777	26.5	1,0,0	1.65	0.79	vs
0.795	6.8	1,0,1			
0.849	10.7	1,0,2	1.75	0.84	vw
0.933	63.5	1,0,3	1.95	0.93	m
1.03	4.3	0,0,6			absent
1.16	24.8	1,0,5	2.57	1.23	w
1.35	12.5	1,1,0	2.92	4.41	w
1.38	3.7	0,0,8			
1.39	6.9	1,1,2			
1.64	6.4	2,0,3	3.45	1.65	w
1.67	3.7	1,1,6			
1.77	4.1	2,0,5			
1.93	5.1	1,1,8			
2.12	4.02	2,1,3	4.62	2.20	w

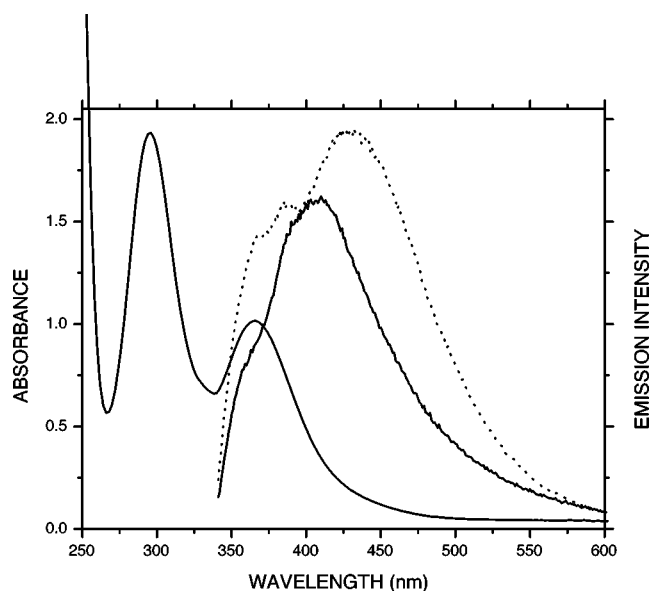


FIG. 3. Absorption and emission spectra of WS₂ nanoclusters. Shown are the absorption spectrum in octane (solid curve on left), emission spectrum in octane (dotted curve) and the emission spectrum in acetonitrile (solid curve on right). The emission spectra were excited at 312 nm.

the possibility that some of the observed absorption is due to rapidly relaxing surface states.

While the absorption spectra of these nanoclusters are the same in the octane and acetonitrile environments, the static and time-resolved emission studies reveal differences in the relaxation dynamics, as discussed below. The emission spectra of the WS₂ nanoclusters in octane and acetonitrile are also shown in Fig. 3. The octane spectrum has a diffuse peak centered at ~430 nm, and a broad shoulder at <400 nm. The acetonitrile emission spectrum has a broad maximum at 410 nm and a much weaker shoulder at wavelengths <400 nm. It is tempting to correlate the 364 and 295 nm absorption maxima with the *A* and *B* excitons observed in bulk WS₂ absorption spectrum. An analogous assignment has been made in the MoS₂ case.^{27(b)} However, the static and time resolved emission polarization results indicate that at least in the WS₂ case, this assignment is not correct. The emission polarization may be characterized by the anisotropy, *r*, given by

$$r = (I_{\text{par}} - I_{\text{per}}) / (I_{\text{par}} + 2I_{\text{per}}), \quad (1)$$

where *I*_{par} and *I*_{per} are the emission intensities having polarizations parallel and perpendicular to that of the absorbed light, respectively.³⁸ The anisotropy is a function of both excitation and emission wavelengths and these dependencies are shown in Fig. 4. The excitation wavelength for the emission anisotropy spectrum was chosen to be 312 nm because this is the wavelength used for the time resolved studies. In both acetonitrile and octane, the emission has an anisotropy maximum on the red edge of the spectra, $\lambda > 460$ nm. The emission anisotropy excitation spectrum shows a maximum at about 385 nm and decreases at further blue excitation wavelengths. There is also a slight decrease at excitation wavelengths to the red of 385 nm. Plots of the emission anisotropy as a function of time for the acetonitrile and oc-

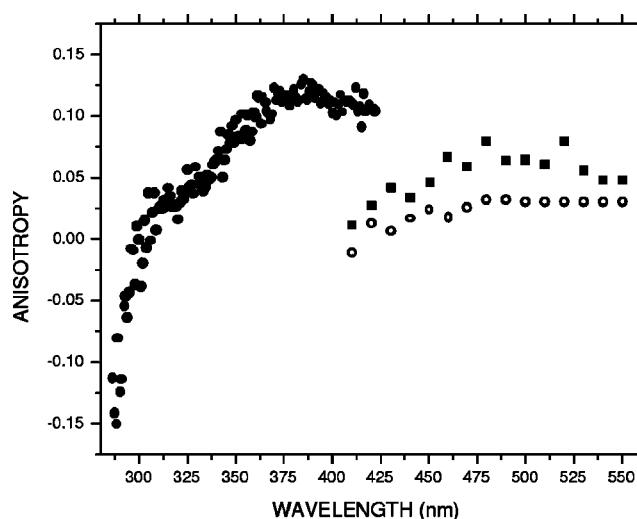


FIG. 4. Plots of the static emission anisotropy versus detection wavelength for WS₂ nanoclusters in acetonitrile (open circles) and in octane (filled circles) and as a function of excitation wavelength in octane (filled squares). The excitation wavelength used for the emission dependence was 312 nm, and the detection wavelength used for the excitation dependence was 495 nm.

tane samples are shown in Fig. 5. If the absorption and emission oscillators are linear and aligned, then an initial anisotropy of 0.40 is predicted from photoselection theory. Similarly, if the absorption and emission oscillators are planar oscillators, then an initial anisotropy of 0.10 is obtained. Figure 5 shows that in both the acetonitrile and octane cases, the initial amplitude of the anisotropy is larger than 0.10 and subsequently decays. Thus, the absorption and emission transitions cannot be due to two-dimensional planar oscillators corresponding to the *A* and *B* excitons. This conclusion is consistent with static (time integrated) anisotropy values

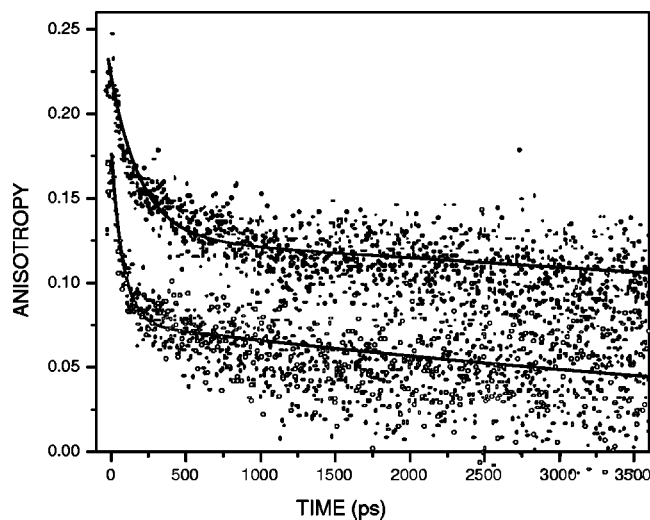


FIG. 5. Time-resolved emission anisotropy of WS₂ nanoclusters in acetonitrile (open circles) and in octane (filled circles). The excitation and detection wavelengths were 312 and 460 nm, respectively. Also shown are calculated biexponential decays. The lower curve corresponds to fast and slow components of 100 ps (amplitude=0.098) and 13 ns (amplitude=0.075), while the upper curve corresponds to fast and slow components of 200 ps (amplitude=0.108) and 20 ns (amplitude=0.127).

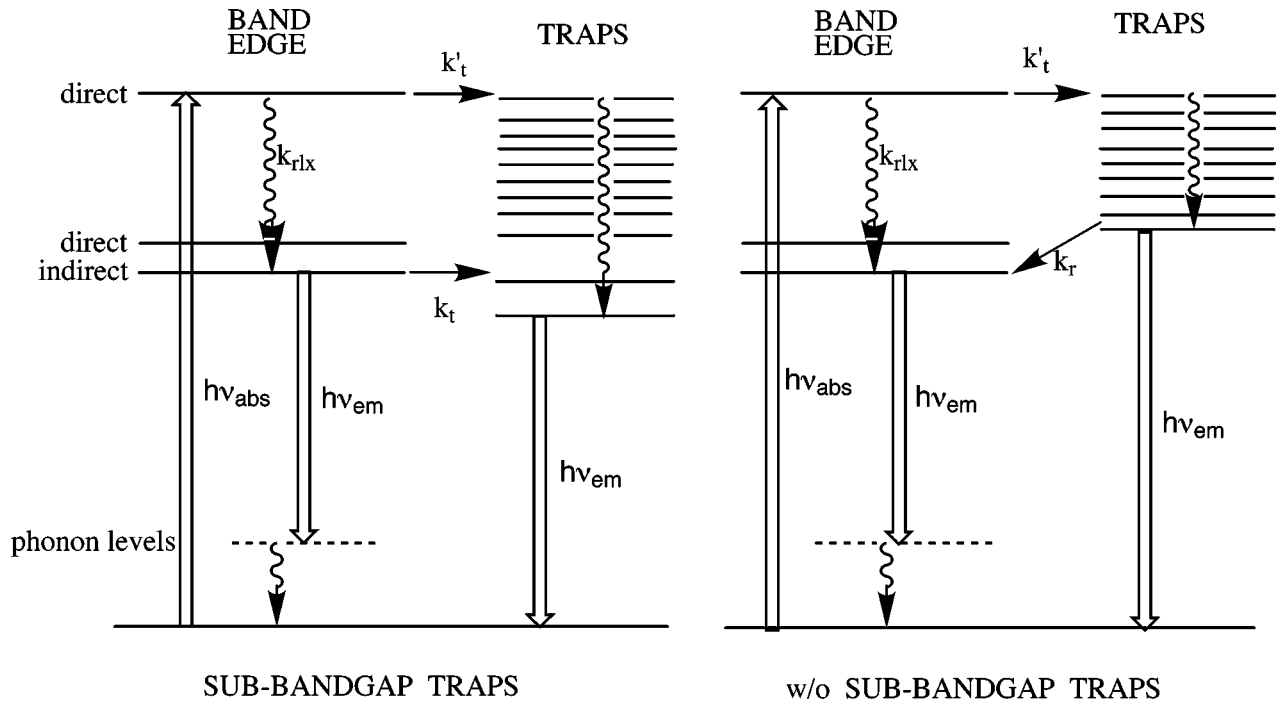


FIG. 6. Schematic diagram of the relaxation processes in WS_2 nanoclusters. Samples consist of a mixture of nanoclusters which do and do not have subband-gap traps. The left side refers to nanoclusters having traps at an energy lower than the band edge, while the right side refers to nanocluster lacking these traps.

larger than 0.10 seen in the anisotropy excitation spectrum, Fig. 4. It could be argued that 312 nm excitation is on the red edge of the 295 nm peak and that this red edge excitation photoselects the long axis of noncircular nanoclusters. However, this hypothesis incorrectly predicts that there would be no long axis selection and thus a smaller anisotropy (by a factor of about 0.1/0.4) following excitation on the blue edge of the 364 nm peak. We conclude that most of the absorption of the 364 nm peak and the red edge of the 295 nm peak is polarized parallel to the crystallographic c axis, perpendicular to the plane of the disk-shaped nanocluster. The negative polarization at wavelengths below 300 nm indicates that there is also an absorption contribution from an in-plane polarized transition in this spectral region. There may also be a small in-plane or isotropically polarized contribution to the red edge of the 364 nm peak, as indicated by the slight decrease in the anisotropy excitation at wavelengths longer than 385 nm.

Figure 4 also shows that the red edge of the emission spectrum (>460 nm) is more polarized than the further blue emission. It follows that the band-edge emission is to the red of the trap state emission. This is a remarkable result, and in sharp contrast to what is observed in other types of nanoclusters. We suggest that this result may be understood in terms of WS_2 being an indirect band gap semiconductor. Specifically, we suggest that the absorption maximum at 364 nm corresponds to the lowest energy allowed (direct) exciton and that the onset of a slightly lower energy transition is buried under this peak. It may be that this transition is momentum forbidden in bulk WS_2 , and gains finite oscillator strength because of the small size of the nanocluster. Polarized emission occurs from this state and most of the emission intensity is to the excited phonon levels needed to conserve

momentum, resulting in a large red shift of the emission maximum. This situation is depicted in Fig. 6.

We suggest that the emission anisotropy decays because of electron and hole trapping and unpolarized emission resulting from the radiative recombination of trapped electrons and holes. Unpolarized emission from trapped electrons and holes allows us to comment on the nature of the traps. In the approximation that the potentials of the electron and hole traps have reflection symmetry with respect to the plane of the nanocluster, the wave functions of the trapped electrons and holes are symmetric in this plane. In this case, the c -axis component of the dipole moment operator is zero and the only nonzero components are in the nanocluster plane. This situation would result in the trap state emission being polarized in the plane of the nanocluster. However, there are dangling bonds which may act as electron and hole traps at the nanocluster edge, and truncation of the crystal structure is expected to result in very unsymmetrical potentials. Thus large electric fields are expected in the vicinity of the electron and hole traps, and the direction of these fields will depend on the local structure of the truncated nanocluster. As a result, the trapped electrons and holes are not expected to have reflection symmetry and the dipole moment operator is expected to have large c -axis components. The lack of reflection symmetry rationalizes the almost unpolarized emission from trapped electrons and holes.

Trap-state and band-edge emission kinetics

The above polarization assignments of the band-edge and trap state emissions make it possible to selectively observe either band edge or trap state emission. Thus, the kinetics of the polarized emission give the time dependence of the band-edge state and trap state populations. In general, emission at

any wavelength will have both polarized (band edge) and unpolarized (trap state) components. The unpolarized component has intensities of parallel and perpendicular polarized emissions which are same. The polarized component has intensities of parallel and perpendicular polarized emissions which are different, with the intensity ratio depending on the anisotropy of the polarized oscillator. The intensity of the unpolarized trap state emission can be expressed in terms of the parallel and perpendicular components of the total emission, if the anisotropy of the polarized component is known. Specifically,

$$I = 3/2I_{\text{prep}} - 1/2I_{\text{par}} \quad (\text{linear polarized oscillator}), \quad (2a)$$

$$I = 4I_{\text{perp}} - 3I_{\text{par}} \quad (\text{planar polarized oscillator}), \quad (2b)$$

where I is the intensity of the unpolarized, trap state component of the emission, and I_{perp} and I_{par} are the perpendicular and parallel emission intensities. Equations (2a) and (2b) correspond to the polarized, band-edge emission component having an anisotropy of 0.4 or 0.1, respectively. Figure 5 shows that the actual value (obtained from the initial, $t=0$, anisotropy) is intermediate between 0.1 and 0.4. The time dependence of the trap state population may be obtained from the polarized emission kinetics, using Eqs. (2a) and (2b). In acetonitrile samples, having little band-edge emission, Eqs. (2a) and (2b) give almost indistinguishable trap state emission decay curves.

The trap state emission kinetics obtained from Eqs. (2a) and (2b) give insight into the trapped electron/hole recombination dynamics, and therefore into the nature of the trap states. Electron and hole traps may be described by a simple excitonlike model as discussed for the case of MoS₂, in a previous publication.²⁸ This model takes the hole (electron) traps to be partially uncompensated negative (positive) charges at the edges of these disklike nanoclusters. The recombination kinetics of trapped electrons and holes can be described by a distributed kinetics model. This model is based on the following assumptions and approximations: (1) Electron and hole trapping, as well as trap-to-trap relaxation, are fast compared to electron/hole recombination; (2) prior to any recombination, trapped electrons and holes are distributed randomly on the edges of the disklike (assumed circular) nanocluster; and (3) the radiative and nonradiative recombination rates are given by the product of a separation-independent term and an exponential dependence of the electron/hole separation. From the above approximations, it follows that the positions of electrons and holes are considered to be fixed as recombination occurs. This results in a time dependent distribution of electron/hole separations which is given by:

$$P(r,t) = [1 - (r/d)^2]^{-1/2} \exp(-[k_r(r) + k_{nr}(r)]t), \quad (3)$$

$$0 < r < d,$$

where r is the electron/hole separation, d is the nanocluster diameter, and $k_r(r)$ and $k_{nr}(r)$ are the separation-dependent radiative and nonradiative recombination rate constants. The electron effective mass is less than that of the hole in MoS₂, with the result being that the trapped electron is more delocalized than the trapped hole. Thus, the distance dependen-

cies of the nonradiative and radiative rates are determined mostly by the spatial extent of the trapped electron. Specifically,

$$k_{nr}(r) = |V|^2 \exp(-2r/a_0), \quad k_r(r) = |\mu|^2 \exp(-2r/a_0) \quad (4)$$

where V and μ are the Franck-Condon weighted matrix elements for nonradiative and radiative decays, respectively, and a_0 is the trapped electron Bohr radius. The above are limiting-case approximations. In particular, we will discuss the rapid trapping and relaxation approximation below. With this model for the time-dependent distribution of electron/hole separations, the time-dependent emission intensity is given by

$$I(t) = \int_0^d k_r(r) P(r,t) dr. \quad (5)$$

The above model has two adjustable parameters: a_0 and the quantity $(|V|^2 + |\mu|^2)$. Because of the integration in Eq. (5), the model actually specifies the a_0 values in terms of a fraction of the nanocluster diameter, a_0/d . Otherwise stated, it is the a_0/d ratio that determines the extent to which the trap state emission decay is nonexponential. a_0 values (in nanometers) are then determined, knowing the nanocluster diameter. If the electron trap is taken to be a full uncompensated charge, then the value of a_0 may be calculated using the dielectric properties of the bulk semiconductor. In general, however, a_0 must be viewed as an adjustable parameter. This model is found to give quantitative agreement with the experimental decays of MoS₂ nanoclusters with a_0 values of about 2.1 nm, in good agreement with the 2.0 nm estimate of a_0 based on a simple excitonlike model of the electron traps.²⁴

In the absence of subband gap traps, the band edge kinetics are determined by the rate of band-edge electron/hole recombination and are very simple. The extent of electron/hole overlap is not expected to be a strong function of particle size, so this rate is also not expected to be a strong function of particle size and the recombination kinetics are expected to be close to single exponential. When subband-gap traps are present, the lifetime of the band-edge state is determined by the trapping rate.

Nanocluster relaxation and trapping dynamics

The emission decay kinetics for the WS₂ nanoclusters in acetonitrile and in octane are shown in Figs. 7, 8, and 9. The emission may be assigned to a wavelength dependent combination of polarized and unpolarized emissions, originating from the nanocluster band-edge and trap states, respectively. These kinetics may be understood in terms of Fig. 6. Following Fig. 6, nanoclusters may be divided into two categories: those which have trap states at an energy below the indirect band edge (left side of Fig. 6), and those which do not (right side of Fig. 6). Most of the nanocluster population falls into the former category (left side of Fig. 6). Nanoclusters having subband gap traps (left side of Fig. 6) exhibit fairly complicated dynamics. Following photoexcitation above the indirect band edge, relaxation to the band edge competes with trapping into high lying trap states. Some fraction of the

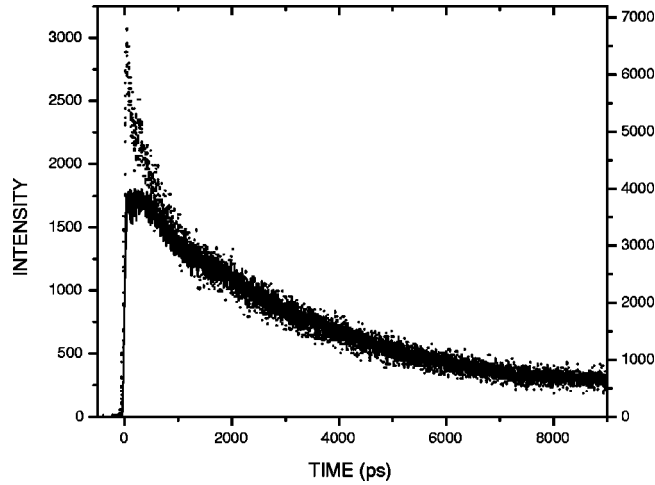


FIG. 7. Emission kinetics of WS_2 nanoclusters in acetonitrile. The plotted data correspond to the unpolarized component of the emission, calculated from the parallel and perpendicular components of the emission decays. The excitation wavelength was 312 nm and detection wavelengths were 360 and 380 nm for the dotted and solid line curves, respectively. The curves are seen to be identical at longer times, and differ in the first few hundred picoseconds in which the 360 nm curve exhibits a rapid decay and the 380 nm curve exhibits a slow rise.

population relaxes through the trap state manifold and populates the lowest energy trap states. The fraction of the population which undergoes trapping to these high lying traps depends on the relative values of k'_t and k_{rlx} . This type of trapping may be fairly efficient because of the high density of trap states at these high energies. The remainder of the population relaxes to the band-edge state. Trapping occurs from the band-edge state with a rate constant k_t , and band-

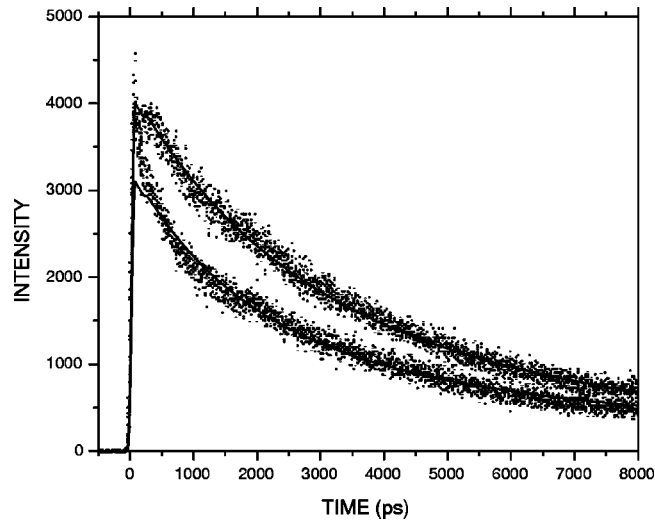


FIG. 8. Emission kinetics of WS_2 nanoclusters in acetonitrile. The plotted data correspond to the unpolarized component of the emission, calculated from the parallel and perpendicular components of the emission decays. The excitation wavelength was 312 nm and detection wavelengths were 380 nm (top curve) and 420 nm (bottom curve). Also shown are curves calculated from the distributed kinetics model with a_0 values of 7.0 nm (top curve) and 4.2 nm (bottom curve). The calculated curves were convolved with the instrument response function.

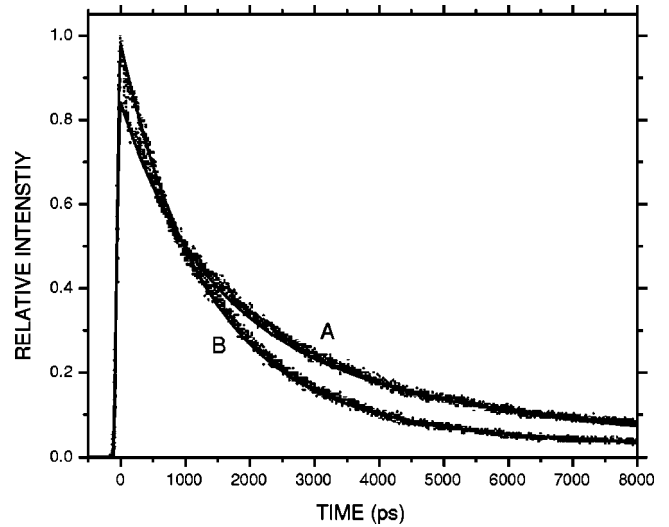


FIG. 9. Total (unpolarized) emission kinetics of WS_2 nanoclusters in octane. The excitation wavelength was 312 nm and detection wavelengths were 380 nm (A), and 480 nm (B). Also shown are curves calculated from the distributed kinetics model and a single exponential decay. Curve A corresponds to only the distributed kinetics model ($a_0=4.2$ nm). Curve B corresponds to a 32% contribution from the distributed kinetics model ($a_0=4.2$ nm) and a 68% contribution of a 1.25 ns decay. Both calculated curves were convolved with the instrument response function.

edge emission is replaced with trap state emission at that rate. This process therefore causes a loss of emission polarization, and the anisotropy decays at the rate k_t . We note that because of the high density of trap states at higher energies, k'_t may be very large, and much larger than k_t . In this scheme there are two distinct ways in which subband-gap traps may be populated: by relaxation to the band edge followed by trapping, and by trapping prior to relaxation followed by relaxation through the trap state manifold.

Nanoclusters lacking subband-gap traps (right side of Fig. 6) exhibit simpler dynamics. In this case, population of high lying trap states is also followed by rapid relaxation through the trap state manifold. When there are no subband-gap traps, this is followed by repopulation of the band edge state. This process provides another mechanism of relaxation to the band-edge state. As a result, the furthest blue unpolarized emission is expected to decay with a rate k_r . The band-edge emission subsequently exhibits single exponential decay kinetics, with a lifetime determined by the rate of nonradiative electron/hole recombination. In this case, the emission anisotropy decays slowly, due to the slow rate of nanocluster rotational diffusion. If the Franck-Condon factors for trapping and detrapping are comparable (a reasonable approximation), then their relative rates will be determined by the density of receiving states. In the trapping case, there are expected to be several sub-bandgap traps on each nanocluster. For the relaxation to the band-edge state, there will be only the discrete, delocalized electronic states. Thus the rate of band-edge repopulation from the high lying trap states is expected to be roughly comparable to the rate of trapping from the band-edge state.

The kinetics of 360 and 380 nm trap state (unpolarized) emission are shown in Fig. 7. These kinetics are obtained from the parallel and perpendicular emission decay kinetics

using Eq. (2a). The 360 nm kinetics corresponds to the blue edge of the observed emission spectrum, see Fig. 3. This emission shows a strongly biphasic decay, with a fast component in the first few hundred picoseconds and a slower component over the next several nanoseconds. The 380 nm decay shows a slow rise for the first few hundred picoseconds, followed by a slow decay, identical to that observed at 360 nm. These emission transients may be assigned to a wavelength dependent combination of emissions from trap states just above and just below the band edge which cannot be completely spectrally separated. The fast component of the 360 nm kinetics is assigned to emission from the trap states above the band edge in nanoclusters lacking subband-gap traps. This emission decays with a rate constant of k_r . The slow component of the 360 nm decay and most of the 380 nm transient is assigned to trap states just below the band edge. The 380 nm emission exhibits a slow rise which is due to slow trapping from the band edge, with a rate of k_t . This rise takes place on the same time scale of a few hundred picoseconds as the 360 nm decay. These results establish that k_r and k_t are of comparable magnitude and that both trapping and detrapping occur on the time scale of a hundred to a few hundreds of picoseconds. We note that while these results indicate that trapping from the band-edge state occurs slowly, Fig. 8 shows that even at redder wavelengths, most of the trap state emission appears rapidly, in less than 50 ps. The above observations indicate that in these acetonitrile samples, a significant mechanism by which traps are populated is through rapid trapping into high lying trap states followed by relaxation in the trap state manifold, rather than by trapping from the band-edge state. As stated above, the faster trapping at the higher energies may be rationalized in terms of a higher density of trap states at the higher energies.

The unpolarized [Eq. (2a)] 380 and 420 nm emission kinetics in acetonitrile are shown in Fig. 8. These kinetics exhibit an initial, 100–200 ps transient due to the trapping dynamics, followed by a nonexponential decay. The nonexponential decay may be accurately fit using the distributed kinetics model and a_0 values of 1.0 and 0.6 of the nanocluster diameter, corresponding to electron Bohr radii of approximately 7.0 and 4.2 nm, respectively. The difference in a_0 values indicates that the traps which emit further to the blue are more spatially diffuse than those which emit further to the red. This is consistent with the above excitonlike model of the trapped electrons in which the shallowest traps emit furthest to the blue and are the most spatially diffuse.

Octane samples exhibit emission which is more intense and more polarized than the acetonitrile samples. These differences may be understood in terms of trap passivation reducing the fraction of nanoclusters having subband-gap traps and a larger contribution to the dynamics corresponding to the right side of Fig. 6. Passivation of the deepest traps has the effect of increasing the fraction of nanoclusters having no subband-gap traps (right side of Fig. 6) and increasing the intensity of the long-lived band-edge emission. The effects of increased band-edge emission in the 420–480 nm region are apparent in the emission kinetics, see Fig. 9. A large fraction of single exponential decay is required to fit the kinetics in this wavelength range. The observed 480 nm decay is accurately fit with a 68% single exponential compo-

nent and a 32% distributed kinetics component. The blue (<420 nm) emission is primarily from trap states, and therefore less polarized than the 420–480 nm emission. In agreement with this assignment, the 380 nm emission kinetics may be accurately fit with the distributed kinetics model (without any single exponential component), using an a_0 value of 4.2 nm. This value is in agreement with the range of a_0 values (7.0 nm at 380 nm and 4.2 nm at 420 nm) used to fit the acetonitrile kinetics.

As stated above, the experimentally observed difference between emission from the band-edge state and trap states is the polarization of the band-edge emission. The trapping dynamics may therefore be elucidated from the decay of the emission anisotropy. Plots of the emission anisotropy as a function of time are shown in Fig. 5. In both the acetonitrile and octane cases, the anisotropy may be approximately fit to a biphasic decay. The magnitudes and decay rates of both decay components may be qualitatively understood in terms of Fig. 6. The band-edge state decays with a rate of k_t , and the fast component of the anisotropy decay is assigned to this process. The values of k_t depends on the density of subband-gap traps. In the octane case, there are comparatively few subband-gap traps and this decay occurs more slowly than in the acetonitrile case. Figure 5 shows that these components decay on approximately the 100 ps time scale, which is comparable to the 75 ps TCSPC response function. As a result, the finite instrument response affects the observed kinetics. Accurate values of the initial anisotropy and the rate of its fast decay may be extracted from these kinetics by the following deconvolution procedure. The short time (<500 ps) behavior of the parallel and perpendicular emission decay curves are fit to biexponentials that have been convolved with the known instrument response. The initial anisotropy kinetics are then obtained from Eq. (1), using these functions (prior to convolution) for I_{par} and I_{per} . This procedure yields decay times of 70 ps and 185 ps for acetonitrile and octane samples, respectively. These values are only slightly faster than the directly observed (prior to any deconvolution) 100 ps and 200 ps decay curves shown in Fig. 5.

The slow component of the anisotropy decay is due to long-lived band-edge emission that depolarizes as the nanoclusters undergo rotational diffusion. The magnitudes of the slowly decaying components in Fig. 5 depend on the trap densities. In the acetonitrile samples, few nanoclusters lack subband-gap traps, and very little of the long-lived anisotropy component is observed. The opposite is true for the octane samples. This result is consistent with the larger magnitude of the static anisotropy observed for the octane samples (Fig. 4).

The decay times of the long-lived anisotropy components are somewhat difficult to determine accurately because of the limited time scale of these experiments, but are approximately 20 and 13 ns in octane and acetonitrile, respectively. This anisotropy decay is assigned to rotational diffusion of the nanoclusters. Nonspherical nanoclusters are expected to give a nonexponential anisotropy decay kinetics. Specifically, an oblate particle is expected to give a biexponential anisotropy decay. However, the nonexponential nature of the decays cannot be resolved from these data, and the long-lived decay components of these data are fit to a single exponential decay. This amounts to approximating the particles

as being spherical. Despite this approximation, approximate rotational diffusion rates may be calculated from Stokes-Einstein considerations using the bulk solvent viscosities.³⁹ With this approximation a hydrodynamic diameter of 6.6 nm is obtained from the anisotropy decays in both acetonitrile and octane. This value of the nanocluster diameter is in agreement with that obtained from the TEM images shown in Fig. 1.

We note that the trapping observed here occurs much more slowly than the femtosecond trapping which has been previously observed in metal oxide,^{40(a)} CdS,^{40(b),41} and CdSe (Refs. 42–44) semiconductor nanoclusters. We speculate that this is due to the difference in phonon frequencies and the nature of the bonding in WS₂ compared to that in metal oxides or CdS and CdSe. Band gap excitation in WS₂ is nominally a nonbonding to nonbonding transition, while it is a bonding to antibonding transition in metal oxides.²¹ As a result, there is a much smaller electron-phonon coupling in these nanoclusters compared to metal oxide nanoclusters. The comparatively low phonon frequencies along with the small electron-phonon coupling may result in slow radiationless processes such as electron and hole trapping.

The above discussion has been vague regarding whether ‘trapping’ refers to electron trapping or hole trapping. It is expected that either electron or hole trapping could result in partial or total loss of emission polarization. In this case, the trapping process depicted in Fig. 6 corresponds to the either electron or hole trapping, and the net rate at which depolarization occurs is the sum of the electron and hole trapping rates. However, based on the excitonlike model of trapped electrons given above, it could be argued that the trapped electrons and holes are somewhat spatially diffuse, and not strongly influenced by the fields at the nanocluster edge. If this is the case, then electron or hole trapping might not result in complete emission depolarization. In this scenario, trapping of one carrier would result in partial depolarization, and subsequent trapping of the other carrier would further depolarize the emission. Close inspection of Fig. 5 (especially the octane kinetics) reveals that there are decay components which are both faster and slower than the calculated 200 ps curve. This may be indicative of different rates associated with electron and hole trapping. Furthermore, it may be possible to resolve the roles of electron and hole trapping by careful analysis of the polarized emission kinetics of bare nanoclusters compared with nanoclusters having adsorbed electron acceptors. These studies are in progress and a preliminary account has recently appeared.⁴⁵ No definite assignment of the roles of electron versus hole trapping can be made based on the results presented here.

CONCLUSIONS

Several conclusions may be drawn from the results presented here.

(1) WS₂ nanoclusters may be synthesized using inverse micelle methods. These nanoclusters have diameters of about 4–7 nm, and have the same crystal structure as bulk WS₂. The electron diffraction results indicate that the particles are single trilayer disks.

(2) Trap state and band-edge emissions have different polarization characteristics. Emission from trapped electrons and holes is unpolarized. Emission from the band edge is polarized and exhibits an anisotropy of about 0.24. Some trapping occurs rapidly, and the actual band edge emission anisotropy may be higher than this value.

(3) The static and time resolved polarization spectra indicate that the lowest observed transitions are polarized along the *c* axis, perpendicular to the plane of the nanocluster. This means that these transitions cannot correlate to the *A* and *B* excitons of bulk WS₂.

(4) WS₂ nanoclusters have a density of subband-gap traps that depends on the synthetic conditions and the chemical treatment of the nanoclusters. Nanoclusters extracted into acetonitrile have a high trap density and very few have no subband-gap traps. As a result, acetonitrile samples exhibit very little band-edge emission. Nanoclusters grown in, or subsequently extracted into an octane phase have a lower trap density and a larger fraction have no subband-gap traps. These samples exhibit long lived (about 1.25 ns) band-edge emission.

(5) Trapping from the band-edge state occurs on the 100 ps time scale and varies with the density of subband-gap traps. Relaxation into the trap states occurs faster in the acetonitrile samples, compared to the octane samples. The present studies do not resolve electron versus hole trapping dynamics.

ACKNOWLEDGMENTS

This work was supported by a grant from the Department of Energy (Grant No. DE-FG03-96ER14717). Partial support for this work was also provided by a grant from the Department of Energy, administered through Sandia National Laboratories. The authors also thank Professor Christer Aakeroy for his help with the crystallographic calculations and in interpreting the electron diffraction results.

*Present address: NSF/Center for Micro-Engineered Materials, 203 Farris Engineering Center, University of New Mexico, Albuquerque, NM 87131

†Author to whom correspondence should be addressed; Email: dfkelley@ksu.edu

¹For a comprehensive review, see *Semiconductor Nanoclusters: Physical, Chemical and Catalytic Aspects*, edited by P. V. Kamat and D. Meisel (Elsevier, Amsterdam, 1997).

²R. Rosetti, J. E. Ellison, J. M. Gibson, and L. E. Brus, *J. Chem. Phys.* **80**, 4464 (1984).

³M. V. Rama Krishna and R. A. Friesner, *J. Chem. Phys.* **95**, 8309 (1991).

⁴P. E. Lippens and M. Lannoo, *Phys. Rev. B* **39**, 10 935 (1989).

⁵Y. Kayanuma, *Phys. Rev. B* **38**, 9797 (1988); **44**, 13 085 (1991).

⁶R. Rossetti, S. M. Beck, and L. E. Brus, *J. Am. Chem. Soc.* **106**, 980 (1984).

⁷R. Kortan, R. Hull, R. L. Opila, M. G. Bawendi, M. L. Steigerwald, P. J. Carroll, and L. E. Brus, *J. Am. Chem. Soc.* **112**, 1327 (1990).

⁸L. Spanhel, M. Haase, H. Weller, and A. Henglein, *J. Am. Chem.*

- Soc. **109**, 5649 (1987).
- ⁹A. Eychmüller, A. Mews, and H. Weller, *Chem. Phys. Lett.* **208**, 59 (1993); A. Mews, A. Eychmüller, M. Giersig, D. Schooss, and H. Weller, *J. Phys. Chem.* **98**, 934 (1994).
- ¹⁰A. Eychmüller, A. Hässelbarth, L. Katsikas, and H. Weller, *Ber. Bunsenges. Phys. Chem.* **95**, 79 (1991).
- ¹¹Y. Tian, T. Newton, N. A. Kotov, D. M. Guldi, and J. Fendler, *J. Phys. Chem.* **100**, 8927 (1996).
- ¹²H. C. Youn, S. Baral, and J. H. Fendler, *J. Phys. Chem.* **92**, 6320 (1988).
- ¹³M. Danek, K. F. Jensen, C. B. Murray, and M. G. Bawendi, *Chem. Mater.* **8**, 173 (1996).
- ¹⁴K. A. Littau, P. J. Szajowski, and L. E. Brus, *Science* **262**, 1242 (1993).
- ¹⁵M. A. Hines and P. Guyot-Sionnest, *J. Phys. Chem.* **100**, 8927 (1996).
- ¹⁶B. O. Dabbousi, J. Rodriguez-Viejo, F. V. Mikulec, J. R. Heine, H. Mattoussi, R. Ober, K. F. Jensen, and M. G. Bawendi, *J. Phys. Chem. B* **101**, 9463 (1997).
- ¹⁷T. Dannhauser, M. O'Neil, K. Johansson, D. Whitten, and G. McLendon, *J. Phys. Chem.* **90**, 6074 (1986).
- ¹⁸M. G. Bawendi, P. J. Carroll, W. L. Wilson, and L. E. Brus, *J. Chem. Phys.* **96**, 946 (1992); M. G. Bawendi, W. I. Wilson, L. Rothberg, P. J. Carroll, T. M. Jedju, M. L. Steigerwald, and L. E. Brus, *Phys. Rev. Lett.* **65**, 1623 (1990).
- ¹⁹Y. Wang, A. Suna, J. McHugh, E. F. Hilinski, P. A. Lucas, and R. D. Johnson, *J. Chem. Phys.* **92**, 6927 (1990).
- ²⁰S. Monticone, R. Tufeu, and A. V. Kanaev, *J. Chem. Phys.* **102**, 2854 (1998).
- ²¹R. Coehoorn, C. Haas, J. Dijkstra, C. J. F. Flipse, R. A. deGroot, and A. Wold, *Phys. Rev. B* **35**, 6195 (1987); **35**, 6203 (1987).
- ²²F. Levy, *Crystallography and Crystal Chemistry of Materials with Layered Structures* (Reidel, Holland, 1976), p. 2.
- ²³K. K. Kam and B. A. Parkinson, *J. Phys. Chem.* **86**, 463 (1982).
- ²⁴B. L. Evans and P. A. Young, *Proc. R. Soc. London, Ser. A* **284**, 402 (1965).
- ²⁵W. Y. Liang, *J. Phys. C* **6**, 551 (1973).
- ²⁶A. R. Beal, W. Y. Liang, and H. P. Hughes, *J. Phys. C* **9**, 2449 (1976); A. R. Beal and H. P. Hughes, *ibid.* **12**, 881 (1979).
- ²⁷(a) J. P. Wilcoxon and G. A. Samara, *Phys. Rev. B* **51**, 7299 (1995); (b) J. P. Wilcoxon, P. P. Newcomer, and G. A. Samara, *J. Appl. Phys.* **81**, 7934 (1997).
- ²⁸R. Doolen, R. Laitinen, F. Parsapour, and D. F. Kelley, *J. Phys. Chem. B* **102**, 3906 (1998).
- ²⁹F. Parsapour, D. F. Kelley, S. Craft, and J. P. Wilcoxon, *J. Chem. Phys.* **104**, 4978 (1996).
- ³⁰B. T. Langdon, V. J. MacKenzie, D. J. Asunskis, and D. F. Kelley, *J. Phys. Chem. B* **103**, 11 176 (1999).
- ³¹C. I. Butoi, B. T. Langdon, and D. F. Kelley, *J. Phys. Chem. B* **102**, 9635 (1998).
- ³²S. A. Empedocles, R. Neusaser, and M. G. Bawendi, *Nature (London)* **399**, 126 (1999).
- ³³(a) M. R. Nimlos, M. A. Young, E. R. Bernstein, and D. F. Kelley, *J. Chem. Phys.* **91**, 5268 (1989); (b) G. A. Brucker and D. F. Kelley, *J. Phys. Chem.* **91**, 2856 (1987).
- ³⁴D. M. Kaschak, S. A. Johnson, D. Hooks, H.-Nyum Kim, D. M. Ward, and T. E. Mallouk, *J. Am. Chem. Soc.* **120**, 10 887 (1998).
- ³⁵J. Kerimo, D. M. Adams, P. F. Barbara, D. M. Kaschak, and T. E. Mallouk, *J. Phys. Chem. B* **102**, 9451 (1998).
- ³⁶D. Sampson, B. A. Parkinson, and D. F. Kelley (unpublished).
- ³⁷A. Sengupta, B. Jiang, K. C. Mandal, and J. Z. Zhang, *J. Phys. Chem. B* **103**, 3128 (1999); O. I. Micic, L. Zongguan, G. Mills, J. C. Sullivan, and D. Meisel, *J. Phys. Chem.* **91**, 6221 (1987).
- ³⁸A. Albrecht, *J. Mol. Spectrosc.* **6**, 84 (1961).
- ³⁹G. R. Fleming, *Chemical Applications of Ultrafast Spectroscopy* (Oxford, New York, 1986), Chap. 6.
- ⁴⁰(a) J. J. Cavaleri, D. P. Colombo, Jr., and R. M. Bowman, *J. Phys. Chem.* **102**, 1341 (1998); (b) D. E. Skinner, D. P. Colombo, Jr., J. J. Cavaleri, and R. M. Bowman, *ibid.* **99**, 7853 (1995).
- ⁴¹J. Z. Zhang, R. H. O'Neil, and T. W. Roberti, *J. Phys. Chem.* **98**, 3859 (1994).
- ⁴²V. I. Klimov, Ch. J. Schwarz, D. W. McBranch, C. A. Leatherdale, and M. G. Bawendi, *Phys. Rev. B* **60**, R2177 (1999).
- ⁴³V. I. Klimov and D. W. McBranch, *Phys. Rev. Lett.* **80**, 4028 (1998).
- ⁴⁴N. P. Ernsting, M. Kaschke, H. Weller, and L. Katsikas, *J. Opt. Soc. Am. B* **7**, 1630 (1990).
- ⁴⁵J. M. Huang and D. F. Kelley, *J. Chem. Phys.* **113**, 793 (2000).